Agent-Based Simulation of Cortical Microtubule Band Movement in the *Arabidopsis* Zygote

Short title:
Simulation of Microtubule Band Movement

Authors: Tomonobu Nonoyama[1], Zichen Kang[1], Hikari Matsumoto[2], Sakumi Nakagawa[2], Minako Ueda[2], Satoru Tsugawa[1]

1 Department of Mechanical Engineering, Faculty of Systems Science and Technology, Akita Prefectural University, Yurihonjo, Akita, 015-0055, Japan

2 Graduate School of Life Sciences, Tohoku University, Sendai, Miyagi, 980-8578, Japan

*Corresponding author: tsugawa@akita-pu.ac.jp

Keywords: Agent-based model, Arabidopsis zygote, Cortical microtubules, Self-organization, Orientational order

Abstract

Arabidopsis thaliana zygotes form a circumferential cortical microtubule (CMT) band that stays at a constant position from the growing tip. CMT bands support zygote anisotropic growth that is essential to determine the apical-basal axis of the plant body, but how stable CMT bands are maintained remains unclear. We hypothesized that cell surface tension induces CMT reorientation of which the strength was defined as the directional cue (DC). We constructed an agent-based simulation model using the DC and its spatial distribution (DC zone) to determine the range of molecular parameters and the width and movement speed of the DC zone required to form the CMT band. We then developed a data–model correspondence method to determine the range of the parameters which are difficult to observe experimentally. We determined that the DC zone must move with an appropriate speed of mechanical change may exist to form a moving CMT band.

Introduction

In the *Arabidopsis thaliana*, the anisotropic growth of the zygote, the single cell formed by the fusion of the egg and sperm cells in plant sexual reproduction, determines the longitudinal (apical–basal) axis of the resulting plant body because the zygotes undergo unequal division after the anisotropic growth to generate a dome-shaped apical cell that leads to the main body of the plant (Tanaka et al., 2024). During zygote elongation, a cortical microtubule (CMT)

band is formed in the circumferential orientation near the subapical region of the cell guiding the future formed first unequal division plane (Kimata et al., 2016; Kang et al., 2024). Given that the CMT band is maintained within a specific subapical region during cell growth, the CMTs above the band may continuously form while the CMTs below the band are degraded to produce a macroscopic movement of the CMT band. Since the cell shape becomes more isotropic without CMT band with the CMT polymerization inhibitors and the CMT band becomes disappeared in the *yoda* mutant with growth arrest prematurely, the interactive feedback between cell growth and CMT organization must be bidirectional (Kang et al., 2024). Root hairs and pollen tubes also exhibit tip growth, but unlike the zygote, their microtubules are aligned in the longitudinal direction (Braun et al., 1999; Cheung et al., 2008). The elongation rate of root hairs is 18 μm/h, more than 10 times that of the zygote (Kang et al., 2023), which might explain why root hairs do not form a circumferential CMT band. These results suggest that the CMT band must move with an appropriate speed consistent with the cell growth, though the mechanisms involved remain unclear.

Many studies have focused on the mechanical feedback from (to) the microtubule to (from) mechanical stress, as introduced below. One pioneering study explored the similarity between the stress distribution derived from the cell geometry and the CMT orientation (Hamant et al., 2008). This was followed by the experimental finding that CMT-severing proteins cut the CMTs perpendicular to the stress orientation (Uyttewaal et al., 2012), and by many reports of the similarity between stress profiles on the cell surface and the distribution of the CMT orientations (Sampathkumar et al., 2014; Hervieux et al., 2017; Sapala et al., 2018). Among them, one important finding was that CMT increased polymerization in regions of increased tension (Inoue et al., 2017; Hamant et al., 2019), suggesting that CMTs may respond to tensile intensity. More interestingly, the property of default orientation in the absence of tension (Durand-Smet et al., 2020) and a hypothesis that the default formation can be overwritten by tensional cues (Colin et al., 2020) were proposed. The overriding of the CMTs by tension defaults back to normal after 10 h, strongly suggesting that CMTs respond not only to the tension intensity itself but also to the changes or fluctuation in tension (Colin et al., 2021; Moulia et al., 2021). In the present study, we therefore hypothesize that the cell surface tension induces the reorientation of the direction in which CMTs are newly formed. The strength of this reorientation is defined as the directional cue (DC), and its spatial distribution as the DC zone. In previous work, the systematic change of DC induced by cell surface tension changed the default CMT orientation (Mirabet et al., 2018); however, the width and the movement speed of the DC zone were not systematically investigated.

Cellulose synthase enzyme complexes move preferentially on the CMTs (Heath, 1974; Paradez et al., 2006), meaning that the CMTs guide the deposition of cellulose microfibrils and

thus cell growth anisotropy (Baluska et al., 2003; Lloyd & Chan, 2008). CMT dynamics are therefore essentially linked to cell or tissue morphogenesis. The growth speed of the CMTs is faster than their shrinkage speed, so the polymers can grow and thus move in an oriented direction, which is known as treadmilling (Mitchison & Kirschner, 1984; Shaw & Kamyar, 2003). The CMTs interact with each other by “zipping” together, inducing depolymerization (called “induced catastrophe”), or “crossover” one another, depending on their interaction angle (Dixit & Cyr, 2004a; 2004b. Based on these phenomenological observations, there were two main ways to model CMT self-organization (Dumond, 2012; Shi & Ma, 2010). Particle-based simulations assumed that all the CMTs act as agents that can grow or shrink while simultaneously interacting with each other (Tindemans et al., 2010; 2014; Chakrabortty et al., 2018; 2018-2), whereas the probability-based approach involved the computation of the density of growing CMTs (Hawkins et al., 2010). Both of these models revealed a qualitatively similar phase diagram (ordered or disordered states as functions of the model parameters of the CMTs) (Shi & Ma, 2010).

These pioneering studies cannot be directly applied to the single zygote, however. First, the studies were based on closed systems in which the CMTs are packed into a restricted zone, which is not applicable to the elongating zygote because it is an open-ended system due to cell growth. Second, the studies did not take the tensional effect into account, with the exception of the recent work by Mirabet et al. (2018). To address the first challenge, we aimed to determine the effect of various molecular parameters for the fixed DC zone on the open-ended cylinder. To overcome the second issue, we reconstructed an agent-based model of the CMTs with systematic changes in the width and the movement speed of the DC zone to assess the appropriateness of the DC movement, i.e., its ability to form a moving CMT band. Another important challenge was the correspondence between data and model, as the data only show the width and the movement speed of the CMT band while the simulation models often contain too many parameters at the molecular scale. A new research framework is therefore required to extract effective parameters that match the actual data.

In this study, we first defined a CMT dynamic space (CDS) with the width and the movement speed of the moving CMT band from actual data to ensure correspondence between data and model. We then reconstructed an agent-based model of CMTs with DCs derived from the tension of the cylindrical cell surface, with the aim of extracting the model parameter range that best explains the width and the movement speed of the CMT band. We tuned the strength of the tension-responsive ability of the CMTs and found that this parameter affects both the width and the orientational order of the resulting CMT band. Next, we analyzed the effects of the induced-catastrophe rate, the width of the DC zone, and the cell radius. Finally, we systematically modified the movement speed of the DC zone and found that the width and

movement speed of the tension band should be constrained to be consistent with the observed data; otherwise, the CMT band falls behind the input speed. Our simulation suggests that an appropriate speed of mechanical change may exist to form a moving CMT band for building up the apical-basal body axis in the Arabidopsis zygote, which is not present in elongating cells without a CMT band, such as pollen tubes and root hairs.

Methods

To understand the CMT dynamics beneath the membrane of the zygote, we constructed an agent-based simulation, as described below. An analysis of the actual zygote data, introduced later, revealed that the width and movement speed of the CMT band have characteristic values at the zygote elongation stage with cylindrical cell geometry; thus, a cylindrical cell surface was selected for use in this model. The agent-based model incorporated the growth, shrinkage, and interaction events between agents (CMTs), the latter of which included zippering, crossovers, and induced catastrophe, as detailed below. The DC derived from tension and the finite tubulin-pool effect were both taken into consideration.

Agent-based model of CMTs on the cylindrical cell surface

The agent-based model of the CMTs was employed based on previous works (Mirabert et al., 2018; Chakrabortty et al., 2018), as shown in Fig. 1. There are six crucial parameters of CMT dynamics: (1) the growth speed of the plus end, v^+ (Fig. 1A); (2) the shrinkage speed of the plus end, v^- (Fig. 1B); (3) the shrinkage speed of the minus end (treadmilling speed), v^{tm}; (4) the switching rate from shrinkage to growth at the plus end (rescue rate), r_r; (5) the switching rate from shrinkage to growth at the plus end (spontaneous catastrophe rate), r_c; and (6) the nucleation rate of CMTs on the cylindrical surface, r_n. The parameter values are summarized in Table 1. In most simulations, cylindrical cell geometry was used with a radius R and height H. The simulation was iterated N times with the time interval Δt for each step.

Interactions of growing CMTs

In addition to the dynamics of a single CMT, described above, the interactions between growing CMTs were also implemented in the simulation (Tindemans et al., 2010, 2014; Chakrabortty et al., 2018, 2018-2; Hawkins et al., 2010; Shi & Ma, 2010). Three interactions were considered: (1) “zippering”, when the growing CMT changes the direction of its growing front to be parallel to an existing CMT without changing the direction of the existing CMT, which happens when a growing CMT collides with an existing CMT at an angle smaller than 40° (Fig. 1C); (2) “induced catastrophe”, when a CMT begins to depolymerize from the

growing front when it meets an existing CMT at an angle greater than 40° (Fig. 1D); and (3) "crossover", when a growing CMT crosses an existing CMT at an angle greater than 40° (Fig. 1E). Induced catastrophes and crossovers are both equally probable (50% probability) when a growing CMT collides with an existing CMT at an angle greater than 40°.

Time and space units

The typical spatial scale of a zygote is 5 μm in radius (Kang et al., 2023). The unit of length of the CMT segment was considered to be 8 nm, the reported width of a ring of tubulin (Mirabet et al., 2018). The previously reported speed of growth at the plus end was 4.8 μm/min (Tindemans et al., 2010), and the simulation time step was approximately 0.2 s. Most of the simulation iterations comprise 12,000 time steps, corresponding to about 40 min.

DC derived from tension

Owing to the growing and shrinking of the CMT plus and minus ends, the length of the CMT agents can be changed, whereas the orientation of the CMTs does not change by default. With this setup, the DC zone (as shown in brown in Fig. 1C) was defined as the region where the newly adding vector is biased in a horizontal direction with weight b_d:

$$\boldsymbol{r_{n+1}} = \frac{(1-b_d)\boldsymbol{r_n} + b_d\boldsymbol{u}}{\|(1-b_{d)}\boldsymbol{r_n} + b_d\boldsymbol{u}\|} \#(1)$$

where $\boldsymbol{r_n}$ and $\boldsymbol{r_{n+1}}$ are the current and next unit vector of the CMT plus end, respectively, $\boldsymbol{u}$ is a circumferential unit vector, and $\|\cdot\|$ is the standard norm. The calculation of the unit vector was almost the same as in a previous study (Mirabet et al., 2018), except that random fluctuations in the direction of the CMT growth were not considered. The notations of position μ_T and width σ_T of the DC zone were used. The direction of the CMT plus end depends on the position of the plus end, as follows:

(i) The microtubule (MT) plus ends located outside of the DC zone do not change the direction.

(ii) The MT plus ends located within the DC zone change the direction toward the horizontal direction.

Finite tubulin-pool effect

In order to observe the CMT dynamics effectively, a finite tubulin pool proposed by Chakrabortty et al. (2018) was used. The pool limits the CMT length by L_{max}, such that the speed of a growing CMT plus end at any time t is dependent on the total length $L(t)$ of all CMTs in the system:

$$v_{tub}^{+}(t) = v^{+}\left(1 - \frac{L(t)}{L_{max}}\right) \#(2)$$

where $L_{max} = \rho_{tub} A$ is the length of all the existing CMTs on the surface area A and finite tubulin density ρ_{tub}, and v^{+} is the CMT plus-end growth speed without taking the pool into consideration.

Quantification of the width of the CMT band in the data

Based on the work of Kang (2023), the coordinate normalization method was used to fix the zygote position. With this normalization, the cell centerline analyzed in the previous studies (Bastien et al., 2016; Kang et al., 2024) was extracted and the fluorescence intensity of the CMTs within the cell was projected to the centerline. The fluorescence intensity was fitted with the truncated Gaussian distribution as a function of position z on the centerline using the parameters $(\alpha, \beta, \mu, s, b)$ as follows:

$$P(S) = \frac{1}{\sigma} \frac{\varphi\left(\frac{S-\mu}{s}\right)}{\Phi\left(\frac{\beta-\mu}{s}\right) - \Phi\left(\frac{\alpha-\mu}{s}\right)} + b \#(3)$$

where S is the curvilinear coordinate along the cell centerline, and the Gaussian probability density function is $\varphi(S) = 1/\sqrt{2\pi}\exp(-1/2S^2)$ with an average μ and standard deviation s. The cumulative distribution function is $\Phi(S) = 1/2\left(1 + erf\left(S/\sqrt{2}\right)\right)$. The width of the CMT band is defined as $\sigma_{\mathrm{MT}}^{data} = 2s$. Furthermore, the CMT position is defined as $\mu_{MT}^{data} = \mu$.

Quantification of the width of the CMT band in the model

The width of the CMT band in the simulations was calculated by quantifying the cumulative probability function P of the CMT segments larger than the threshold 3.85 μm (1/8 of the circumference); this threshold can omit unorganized CMTs. $P(S)$ was then fitted with a sigmoid curve using five points around $S = 0.5$ (Fig. S1, gray dashed line). The width of the CMT band was estimated by the 68th percentile of the corresponding probability density function for the fitted sigmoidal cumulative distribution (Fig. S1).

Order parameter tensor quantifying the orientational order of the CMTs

To measure the degree of the orientational order of the CMT array in the simulations, a local order parameter tensor $\boldsymbol{q}$ and a global order parameter tensor $\boldsymbol{Q}$ were introduced (Chakrabortty et al., 2018). Using the orientation of the CMT segment at the position x, $\hat{\omega} = \cos\alpha\ \hat{e}_x(x) + \sin\alpha\ \hat{e}_y(x)$ where $\alpha \in [0, 2\pi)$ is the declination angle between $\hat{\omega}$ and $\hat{e}_x$. The local order parameter tensor $\boldsymbol{q}$ at the local area dA is defined as

$$q_{ij} = 2\langle \widehat{\omega_i}\widehat{\omega_j} \rangle - \delta_{ij}, \#(4)$$

with the matrix form

$$\boldsymbol{q} = \begin{bmatrix} (2\cos^2\alpha - 1)e_x \otimes e_x & 2\cos\alpha\,\sin\alpha\, e_x \otimes e_y \\ 2\cos\alpha\,\sin\alpha\, e_y \otimes e_x & (2\sin^2\alpha - 1)e_y \otimes e_y \end{bmatrix}. \#(5)$$

Note that $<\cdot>$ means the sample average of $\cdot$ within the local area dA. The local orientational order and the local orientation of the CMT segments within dA are estimated by the first eigenvalue of q and by the orientation of the corresponding eigenvector of q, respectively. For the characterization of the global orientation, the global order parameter tensor was defined as

$$\boldsymbol{Q} = \frac{\int dA(x)\rho(x)\boldsymbol{q}(\boldsymbol{x})}{\int dA(x)\rho(x)} \#(6)$$

where $\rho(x)$ is the local areal density of the CMT segments within dA. The global orientational order and the global orientation of all the CMTs within the whole region are estimated by the first eigenvalue denoted by Λ of $\boldsymbol{Q}$ and by the orientation of the corresponding eigenvector of $\boldsymbol{Q}$, respectively. Λ becomes 0 for completely random CMT orientations, while for well-organized CMTs, Λ becomes +1 for the horizontal array and −1 for the vertical array. The number of local regions is n_{div} in this study, which divides the whole region into the parts with height H/n_{div}.

Results

The CMT band moves upwards with a speed of 1.5 ± 1.2 µm/min and a width of 5.2 ± 2.4 µm

To determine the mechanism by which the CMT band moves to maintain its position as the zygote expands, we first quantified the width and movement speed of the CMT band using actual observation data (Fig. 2A and 2B). At the CMT-building stage, which occurs just after fertilization, the CMTs would not be well organized yet; subsequently, the cell becomes protruded in the apical direction with CMT band near the cell tip (Kimata et al., 2016). The cell maintains anisotropic elongation during the elongation stage, during which the organized CMT band is localized about 5~7µm below the growing tip. To elucidate how the CMT band is maintained, we focused on the elongating stage assuming a cylindrical cell geometry.

To standardize the dynamics of the CMT bands of different individuals to an appropriate time scale, we used the characteristic time t_{RGS} at the rapid growth stage (RGS), during which the cell length rapidly increased (Kang et al., 2023). We defined the stage from t_0 (5 h before t_{RGS}) to t_{RGS} as the elongating stage. The CMT fluorescence intensity projected on the cell centerline (Fig. 2C and 2D) was fitted by the truncated Gaussian distribution with mean μ_{MT}^{data} and standard deviation σ_{MT}^{data} (Fig. 2E and 2F; see also Methods). The kymograph of the CMT fluorescence intensity revealed that the CMT band is actually localized to the subapical region, maintaining almost the exact same distance to the cell tip as the zygote elongates (Fig.

2G). The width of the CMT band also remained constant at approximately 5.2 ± 2.4 μm during elongation. The movement speed of the CMT band was less than 2.7 μm/h (Fig. 2H).

Tension-responsive ability parameter b_d affects both the width and orientational order of the CMT band

To establish correspondence between the observed data and the model parameters, we introduced a CMT dynamic space (CDS) describing the speed $d\mu_{MT}^{data}/dt$ and the width $\sigma_{MT}^{\mathrm{data}}$ of the CMT band (Fig. 2H). A total of 11 parameters were included in the model (Fig. 1): six CMT dynamics parameters v^+, v^-, v^{tm}, r_r, r_c, and r_n; three mechanical parameters b_d, μ_T, and σ_T; and two geometrical parameters R and H (Table 1). Based on previous studies and the observed data (Chakrabortty et al., 2018-2, Shaw et al., 2003, Eren et al., 2010, Tindemans et al., 2014-2), we set six parameters (v^+, v^-, v^{tm}, r_r, H, and r_n) as fixed and observed the effects of changing the remaining five parameters (r_c, b_d, μ_T, σ_T, and R). We used the CDS to make correspondence with these five parameters.

To observe the effects of parameter perturbations, it is necessary to identify the parameters that can replicate a similar CMT band with sample-averaged data. We initially fixed the parameter μ_T at the specific location $z = 10$ μm within the range of $z \in [0, 20]$ (Fig. 2H) and used specific parameters ($r_c = 0.001$, $b_d = 0.01$, $\sigma_T = 6.67$ [μm], and $R = 5$ [μm]). Using this configuration, we examined the changes in the resulting CMT band by perturbing the parameters (r_c, b_d, σ_T, and R).

To avoid misunderstanding, we defined the terms “single CMT formation” as a single CMT oriented in the circumferential direction (a single ring of CMT) and “CMT band formation” as a band formed in the circumferential direction (a bundled structure of CMTs). We noticed that the CMT band can be formed for the parameter $b_d = 0$, but it was not specifically localized (Fig. 3A). Next, we set $b_d = 0.001$ for the case of the weak DC, resulting in a CMT band partially localized near the DC zone (dashed line) (Fig. 3B). When $b_d = 0.01$, for the case of the strong DC, the formed CMT band covered the whole region of the DC zone (Fig. 3C). To check the time scale of the reorientation during the single CMT formation, we confirmed that, in the cases $b_d < 0.01$, the converging time to the horizontal orientation of the CMTs becomes more than the time scale of single CMT formation roughly estimated as $2\pi R/v_+ \sim 6.5$ min for $R = 5$ μm (Fig. 3D), therefore we set the case $b_d = 0.01$ as strong DC where the converging time is fast enough than the single CMT formation.

To quantitatively describe the degree of CMT band formation, we evaluated the width of the CMT band σ_{MT}^{model}, and the global order parameter Λ, measuring both the orientation and density of the CMTs (see Methods). The order parameter Λ becomes 0 for the completely random orientation of the CMTs and 1 for well-organized CMTs. As a result, we quantitatively

confirmed that the width σ_{MT}^{model} decreases as a function of b_d, consistent with the above qualitative observations (Fig. 3F). Furthermore, we quantitatively confirmed that the order of CMT organization increases as b_d increases, which was also consistent as well (Fig. 3G).

Catastrophe rate induces a phase transition for both strong and weak DC

Next, to confirm the robustness of the CMT band against CMT depolymerization, we systematically increased the catastrophe rate. Since depolymerization shortens CMTs, it is expected to decrease the probability of CMT collisions that may inhibit the formation of CMT bands. Because the DC may compensate for the increased catastrophe rate by facilitating band formation, we tested the changes for the weak and strong DC conditions. In the case of weak DC, the CMT organization at $t = 20$ min becomes sparse as the catastrophe rate increases because the induced catastrophe frequently cuts the CMTs (Fig. S2A). Moreover, the quantitative evaluation of Λ revealed that the degree of orientational order was less than 0.75, meaning that the CMTs are not strongly organized (Fig. S2B). As expected, our definition of the width of the CMT band suddenly dropped to small values at $r_c = 0.002$, where the phase transition in terms of CMT band width occurs (Fig. S2C). This sudden decrease in the width of the CMT band occurs even in the case of the strong DC, where the horizontally aligned single CMT formation was cut by the catastrophe (Fig. S2D). In this case, the index Λ was greater than 0.75, meaning that the CMTs are strongly organized (Fig. S2E) and a similar phase transition occurs (Fig. S2F).

The CMT band widens as the input DC widens under both weak and strong DC

To exlpore whether the width of the output CMT band σ_{MT}^{model} corresponds to the width of the input, we focused on the perturbation of the input DC width σ_T. In the case of weak DC, the CMTs at $t = 20$ min were widely distributed beyond the input DC zone (Fig. 3G). In the case of strong DC, the CMTs at $t = 20$ min were distributed with almost the same width as that of the input DC zone (Fig. 3H). We quantitatively confirmed that these results were preserved independent of the parameter σ_T (Fig. 3I).

Cylinder radius does not strongly affect the CMT band but emphasizes two different types of CMT organization

Adimittingthat changes in the cylinder radius alter the circumference and surface area of the cylinder, which is expected to increase the time required for CMT to form bands, we tested the cases of R = 5.0 μm (typical zygote scale reported by Kang et al. (2023)) and R = 15 μm. In addition, we tested the weak and strong DC conditions because the DC may compensate for a delay in CMT band formation. In the case of strong DC, the CMT band was rapidly

organized, and this behavior was not strongly affected by the radius (Fig. 4A); therefore, the index Λ and the CMT band width σ_{MT} showed a similar trend (Fig. 4A and 4B). On the other hand, in the case of weak DC, the CMTs were broadly distributed across the entire region, and they gradually organized within the DC zone (Fig. 4D and 4E). We call this phenomenon a gradual organization of CMTs and distinguish this from the rapid organization. As a result, the index Λ values are lower than those in the case of strong DC, and the CMT band width σ_{MT} with $R = 15$ μm gradually decreases, reflecting the gradual organization (Fig. 4E). The mechanism behind this might be the different frequency of the CMT encounters. In the case of strong DC, the horizontal CMTs are rapidly organized, preventing the diagonal organization of the CMT band (Fig. 4C). In the case of weak DC, the horizontal CMTs are not well organized, allowing the diagonal or spiral organization of the CMT band (Fig. 4F).

The moving CMT band can be formed when the DC zone displays an appropriate movement speed and width

As the results above suggested that a desired CMT band can be reproduced with $r_c \leq 0.002$, $b_d \geq 0.01$, σ_T slightly smaller than the desired band, and $R = 5.0$, corresponding to the observed data, we are now able to move the designated CMT band by changing the specific parameter $d\mu_T/dt$ (the movement speed of the DC zone). As schematically illustrated in Fig. 5A, we searched for the best fitted parameter set ($d\mu_T/dt$, σ_T) from the CDS in Fig. 2H using an exhaustive search of the model parameters. As the expected DC parameters were unknown, we distributed the parameter set with $d\mu_T/dt \in [0, 4.0]$ μm/h and $\sigma_T \in [0.5, 3.5]$ μm as a similar range to the data. As a result, σ_{MT}^{model} becomes wider than σ_T while unexpectedly the resulting $d\mu_{MT}^{model}/dt$ becomes smaller or sometimes even a negative value, which is below the expected movement speed of the CMT band (Fig. 5B, D, F, H). To demonstrate what happens, we plotted the simulated CMTs in Fig. 5C. (i) shows CMT behaviors with appropriate width and movement speed of the DC zone (Fig. 5D and Fig. 5E). (ii) shows the behavior with slower DC movement (Fig. 5F, G). (iii) shows the behavior with faster DC movement and a wider DC (Fig. 5H). These results suggest that when the DC zone moves faster than the CMT growing speed, the organized CMT band is left behind the DC zone (Fig. 5H and 5I).

In summary, we conclude that the moving CMT band could be achieved with an appropriate width and movement speed of the DC zone.

Discussion

In this study, we developed an agent-based simulation based on the CMT

tension-responsive hypothesis to identify the parameters necessary for the formation of the moving CMT band, which is specifically formed in the plant zygote. Through a CDS analysis, we successfully compared the CMT bands between the model and the observed data to estimate the necessary parameters, and obtained three new main findings regarding the reproduction of the moving CMT band in *Arabidopsis* zygotes. (1) The width of the CMT band was about 5.2 ± 2.4 μm, and the movement speed was about 1.3 ± 1.5 μm/h. (2) There can be two types of CMT band formation: rapid organization and gradual organization. (3) The formation of the moving CMT band requires an appropriate width and movement speed in the input mechanical parameters too.

In addition to the CMT tension-responsive hypothesis, the organization of the CMT band has been hypothesized to involve other mechanisms. The edge catastrophe hypothesis, where the cell edge induces CMT catastrophe, was proposed to explain CMT organization in early embryonic apical cells in previous studies (Chakrabortty et al., 2018; Chakrabortty et al., 2018-2); however, this hypothesis seems unlikely to hold for the zygote, especially in the elongating term, when cell edges are lacking around the CMT band. The conceptual basis for the CMT tension-responsive hypothesis is an increase in the rate of CMT polymerization in the region of higher tension, based on previous studies (Inoue et al., 2016; Hamant et al., 2019), but subsequent experimental research on CMTs in protoplasts (Colin, 2021) has shown that tension changes over time may increase the rate of CMT polymerization. Thus, the driving force might be a time derivative of the tension (Kang et al., 2024). Additionally, we admit that the possibility that CMTs are severed in a direction perpendicular to the tension exerted by katanin outside the DC zone (Uyttewaal et al., 2012) is not ruled out.

For the case of the moving DC zone, in order to be consistent with the parameter ranges of CMT band in the actual observed data, the movement speed of the DC zone must be comparable to that of cell elongation (1.5 μm/h on average). A similar mechanism for a moving ordered structure may exist for the formation of CMT band structure in the tip growth mode in fern protonema, where the elongation rate is small (Murata & Wada, 1989). The elongation rate of root hairs is 18 μm/h, which is more than 10 times that of the zygote (Kang et al., 2023), so it is thought that they are unable to form CMT bands, similar to our numerical result. This is the "left-behind" phenomenon, in which the mechanical (tensional) change during elongation becomes so fast that CMT organization does not catch up with the input mechanical perturbation. As the elongation speed of the pollen tubes is 100–1000 times that of the zygote (Bedinger, 1992; Schiøtt et al., 2004), the reason that they do not have CMT bands is thought to be similar to the left-behind phenomenon. The question of when and how the organisms evolved a moving CMT band should be of great significance, not only for cell and molecular biology, but also for understanding the evolution and diversity of plant cells.

In this study, we developed a data–model correspondence method called CDS to narrow down the range of molecular parameters such as the tension-responsive ability and catastrophe rate of the CMTs, which are difficult to observe experimentally. This method can be applied not only to other cylindrical plant cells (Hasezawa et al., 1997), but also to animal cells in general, such as the orientational order during the formation of the extracellular matrix of animal cells (for example, in the *Drosophila* trachea; Öztürk-Çolak et al., 2016). The interdisciplinary research that links biological images and simulation models can thus provide new opportunities to elucidate and understand the essential dynamics of plant and animal cytoskeletons.

Acknowledgments:

The authors thank Koichi Fujimoto, Katsuyoshi Matsushita and Naoya Kamamoto (Hiroshima Univerisity), Takumi Higaki, and Haruka Ono (Kumamoto University), Ishimoto Yukitaka (Saga University) and Yusuke Kimata (Tohoku University) for helpful discussions.

Author Contributions:

T.N. and S.T. conceived and designed the study. T.N. and S.T. developed and implemented models and algorithms. H.M., S.N. and M.U. carried out data acquisition from live cell imaging. T.N. and S.T. wrote the manuscript. T.N., Z.K., S.T., and M.U. edited and reviewed the manuscript. S.T., H.M., and M.U. provided research funding. All authors have read and approved the manuscript.

Financial Support

This work was supported by the Japan Society for the Promotion of Science [JSPS KAKENHI (JP20K15832 to S.T.), a Grant-in-Aid for Early-Career Scientists (JP22K15135 to H.M.), a Grant-in-Aid for Scientific Research on Innovative Areas (JP19H05670 and JP19H05676 to M.U.), a Grant-in-Aid for Scientific Research (B) (JP23H02494 to M.U.), International Leading Research (JP22K21352 to M.U.)], the Japan Science and Technology Agency [CREST (JPMJCR2121)],, the Suntory Rising Stars Encouragement Program in Life Sciences (SunRiSE; to M.U.), and the Toray Science Foundation (20-6102 to M.U.).

Data Availability Statement

The data supporting the findings of this study are available from the author, Tomonobu Nonoyama, upon a reasonable request.

Competing Interest

The authors have no competing interest.

References:

1. Tanaka, S., Matsushita, Y., Hanaki, Y., Higaki, T., Kamamoto, N., Matsushita, K., Higashiyama, T., Fujimoto, K., Ueda, M. (2024) HD-ZIP IV genes are essential for embryo initial cell polarization in the radial axis initiation in *Arabidopsis*. *Current Biology.* 0960-9822. doi: 10.1016/j.cub.2024.08.03
2. Kimata, Y., Higaki, T., Kawashima, T., Kurihara, D., Sato, Y., Yamada, T., Hasezawa, S., Berger, F., Higashiyama, T., Ueda, M. (2016). Cytoskeleton dynamics control the first asymmetric cell division in Arabidopsis zygote. *Proceedings of the National Academy of Sciences*, 113(49), 14157-14162.
3. Kang, Z. C., Matsumoto, H., Nonoyama, T., Nakagawa, S., Ishimoto, Y., Tsugawa, S., Ueda, M. (2023). Coordinate normalization of live-cell imaging data reveals growth dynamics of the Arabidopsis zygote. *Plant Cell Physiology,* pcad020.
4. Kang, Z. C., Nonoyama, T., Ishimoto, Y., Matsumoto, H., Nakagawa, S., Ueda, M., Tsugawa, S., An elasto-plastic deformation model of hemispherical tip growth in Arabidopsis zygotes. *Submitted*.
5. Kang, Z. C., Nakagawa, S., Matsumoto, H., Ishimoto, Y., Nonoyama, T., Hanaki, Y., Tsugawa, S., Ueda, M. (2024). Material derivative of tension ensures accurate asymmetric cell division of Arabidopsis zygotes, *bioRxiv*.
6. Braun, M., Baluska, F., Witsch, M. V., Menzel, D., (1999). Redistribution of actin, profilin and phosphatidylinositol-4, 5-bisphosphate in growing and maturing root hairs. *Planta*, 209, 435–443
7. Cheung, A. Y., Duan, Q. H., Costa, S. S., Barend, H. J. G., Stillo, V. S., Feijo, J., Wu, H. M., (2008). The Dynamic Pollen Tube Cytoskeleton: Live Cell Studies Using Actin-Binding and Microtubule-Binding Reporter Proteins. *Molecular Plant*, 1(4), 686 - 702
8. Hamant, O., Heisler, M. G., Jönsson, H., Krupinski, P., Uyttewaa, M., Bokov, P., Corson, F., Sahlin, P., Boudaoud, A., Meyerowitz, E. M., Couder, Y., Traas, J., (2008). Developmental patterning by mechanical signals in Arabidopsis. *Science*. 322(5908), 1650-1655.
9. Uyttewaal, M., Burian, A., Alim, K., Landrein, B., Borowska-Wykręt, D., Dedieu, A., Peaucelle, A., Ludynia, M., Traas, J., Boudaoud, A., Kwiatkowska, D., Hamant, O. (2012). Mechanical stress acts via katanin to amplify differences in growth rate between adjacent cells in Arabidopsis. *Cell*. 149(2), 439-451.
10. Sampathkumar, A., Krupinski, P., Wightman, R., Milani, P., Berquand, A., Boudaoud, A., Hamant, O., Jönsson, H., (2014). Meyerowitz. Subcellular and supracellular mechanical stress prescribes cytoskeleton behavior in Arabidopsis cotyledon pavement cells. *eLife*, 3:

e01967.

11. Hervieux, N., Tsugawa, S., Fruleux, A., Dumond, M., Routier-Kierzkowska, A-L., Komatsuzaki, T., Boudaoud, A., Larkin, J. C., Smith, R. S., Li, C-B., Hamant, O. (2017). Mechanical Shielding of Rapidly Growing Cells Buffers Growth Heterogeneity and Contributes to Organ Shape Reproducibility, *Current Biology*. 27(22), 3468-3479.
12. Sapala, A., Runions, A., Routier-Kierzkowska, A-L., Gupta, M. S., Hong, L., Hofhuis, H., Verger, S., Mosca, G., Li, C-B., Hay, A., Hamant, O., Roeder, A. H. K., Tsiantis, M., Prusinkiewicz, P., Smith, R. S. (2018). Why plants make puzzle cells, and how their shape emerges. *eLife*, 7, e32794.
13. Inoue, D., Nitta, T., Kabir, A. M.R., Sada, K., Gond, J. P., Konagaya, A., Kakugo, A., (2016). Sensing surface mechanical deformation using active probes driven by motor proteins. *Nature Communications*, 7, 12557.
14. Hamant, O., Inoue, D., Bouchez, D., Dumais, J., Mjolsness, E. (2019). Are microtubules tension sensors? *Nature Communications*, 10(1), 2360.
15. Durand-Smet, P., Spelman, T. A., Meyerowitz, E. M., Jönsson, H. (2020). Cytoskeletal organization in isolated plant cells under geometry control. *Proceedings of the National Academy of Sciences*, 117(29), 17399-17408.
16. Colin, L., Chevallier, A., Tsugawa, S., Gacon, F., Godin, C., Viasnoff, V., Saunders, T. E., Hamant, O. (2021). Cortical tension overrides geometrical cues to orient microtubules in confined protoplasts. *Proceedings of the National Academy of Sciences*, 117(51), 32731-32738.
17. Moulia, B., Douady, S., Hamant, O. (2021). Fluctuations shape plants through proprioception. *Science*. 372(6540), eabc6868.
18. Heath, I. B., (1974). A unified hypothesis for the role of membrane bound enzyme complexes and microtubules in plant cell wall synthesis. *Journal of Theoretical Biology.* 48(2), 445-449.
19. Paradez, A. R., Somerville, C. R., Ehrhardt, D. W., (2006). Visualization of cellulose synthase demonstrates functional association with microtubules. *Science*. 312(5779), 1491-1495.
20. Balsuka, F. B., Samaj, J., Wojtaszek, P., Volkmann, D., Menzel, D. (2003). Cytoskelen-plasma Membrane-cell wall continuum in plants. Emerging links revisited. *Plant physiology*, 133(2), 482-491.
21. Lloyd, C., Chan, J. (2008). The parallel lives of microtubules and cellulose microfibrils. *Current Opinion in Plant Biology*. 11(6), 641-646.
22. Mitchison, T., Kirschner, M. (1984). Dynamic instability of microtubule growth. *Nature*. 312, 237-242.

23. Shaw, S. L., Kamyar, R., Ehrhardt, D. (2003) Sustained microtubule treadmilling in Arabidopsis cortical arrays. *Science*. 300(5626), 1715-1718.
24. Dixit, R., Cyr, R. (2004). Encounters between dynamic cortical microtubules promote ordering of the cortical array through angle-dependent modifications of microtubule behavior. *Plant Cell*. 16(12), 3274-3284.
25. Dixit, R., Cyr, R. The cortical microtubule array: From Dynamics to Organization. *Plant Cell.* 16(10), 2546-2552.
26. Dumond, M. (2013) Two main ways to model the self-organization of cortical microtubules. *BioSciences Master Reviews in Ecole Normale Superieure de Lyon*.
27. Shi, X-Q., Ma, Y-Q., (2010). Understanding phase behavior of plant cell cortex microtubule organization. *Proceedings of the National Academy of Sciences Sciences.* 107, 11709-11714.
28. Tindemans, S. H., Hawkins, R. J., Mulder, B. M. (2010). Survival of the Aligned: Ordering of the Plant Cortical Microtubule Array. *Physical Review Letters*, 104, 058103.
29. Tindemans S. H., Deinum, E. E., Lindeboom, J. J., Mulder, B. M. (2014). Efficient event-driven simulations shed new light on microtubule organization in the plant cortical array. *Frontiers in Physics* 2, 1-15.
30. Chakrabortty, B., Willemsen, V., Zeeuw, T., Liao, C-Y., Weijers, D., Mulder, B. M., Scheres, B. (2018-1). *Current Biology*, 28(19): 3031-3043.e2.
31. Chakrabortty, B., Blilou, I., Scheres, B., Mulder, B. M. (2018-2). A computational framework for cortical microtubule dynamics in realistically shaped plant cells. *Plos Computational Biology*, 14(2), e1005959.
32. Hawkins, R. J., Tindemans, S. H., Mulder, B. M. (2010). Model for the orientational ordering of the plant microtubule cortical array. *Physical Review E*, 82, 011911.
33. Mirabet, V., Krupinski, P., Hamant, O., Meyerowitz, E., Jönsson, H., Boudaoud, A. (2018) The self-organization of plant microtubules inside the cell volume yields their cortical localization, stable alignment, and sensitivity to external cues. *Plos Computational Biology*, 14(2), 21006011.
34. Bastien, R., Legland, D., Martin, M., Fregosi, L., Peaucelle, A., Douady, S., Moulia, B., Höfte, H. (2016). KymoRod: a method for automated kinematic analysis of rod-shaped plant organs. *The Plant Journal*, 88, 468-475.
35. Shaw, S. L., Kamyar, R., Ehrhardt, D. W. (2003). Sustained Microtubule Treadmilling in Arabidopsis Cortical Arrays. *Science*,300, 1715-1718.
36. Eren, E. C., Dixit, R., Gautam, N. (2010). A Three-Dimensional Computer Simulation Model Reveals the Mechanisms for Self-Organization of Plant Cortical Microtubules into Oblique Arrays, *Molecular Biology of the Cell.* 21:15, 2674-2684,

37. Hasezawa, S., Kumagai, F., Nagata, T., Sites of microtubule reorganization in tabacco BY-2 cells during cell-cycle progression. (1997). *Protoplasma*, 198, 202-209
38. Murata, T., Wada, M. (1989). Organization of cortical microtubules and microfibril deposition in response to blue-light-induced apical swelling in a tip-growing *Adiantum* protonema cell. *Planta.* 178, 334–341.
39. Bedinger, P. (1992). The remarkable biology of pollen. *Plant Cell.* 4(8), 879-87..
40. Schiøtt, M., Romanowsky, S. M., Bækgaard, L., Harper, J. F., (2004). A plant plasma membrane Ca2+ pump is required for normal pollen tube growth and fertilization. *Proceedings of the National Academy of Sciences.* 4101(25), 9502-9507.
41. Öztürk-Çolak, A., Moussian, B., Araújo, S. J., Casanova, J. (2016). A feedback mechanism converts individual cell features into a supracellular ECM structure in Drosophila trachea, *eLife*, 5, e09373
42. Robinson, S., Kuhlemeier, C. (2018). Global Compression Reorients Cortical Microtubules in Arabidopsis Hypocotyl Epidermis and Promotes Growth, *Current Biology.* 28(11).

Tables:

Table 1. Simulation parameters and variables with their default values. The height and radius of the simulation cylinders are based on the observed data in actual *Arabidopsis* zygotes (Kang et al., 2023). The threshold angle of zippering and the probabilities of induced catastrophes and crossover were based on Dixit & Cyr (2004a) and Tindemans et al. (2014b). The strength of the directional cue (DC) was based on Mirabet et al. (2018).

parameter	Value	Meaning
H	20 [μm]	Height of the cylinder
R	5.0-15.0 [μm]	Radius of the cylinder
N	6000,12000	Simulation steps
Δt	0.02 [sec]	Time interval of the simulation steps
v^{+}	0.08 [μm/sec]	Growth speed of the plus end
v^{-}	0.16 [μm/sec]	Shrinkage speed of the plus end
v^{tm}	0.01 [μm/sec]	Shrinkage speed of the minus end
r_r	0.007 [1/sec]	Rescue rate
r_c	0.001-0.01[1/sec]	Catastrophe rate
r_n	0.001 [1/sec]	Nucleation rate
θ^{*}	40 [degree]	Threshold angle of CMT interactions
P_{cat}	0.5	Probability of induced catastrophe
P_{cro}	0.5	Probability of crossover
b_d	0.0001-0.01	Strength of the DC
μ_T	10.0 [μm]	Position of the below end of the DC zone
σ_T	2-10 [μm]	Width of the DC zone

Table1

Figures:

Fig. 1. Schematic illustrations of cortical microtubule (CMT) dynamics, their interactions, and the effect of directional cue (DC). (A) Microtubule (MT) growth, when the CMT plus end grows at speed v^{+}. (B) MT shrinkage, when the CMT plus end shrinks at speed v^{-} while the CMT minus end undergoes shrinkage at speed v^{tm}. Switching rate from growth to shrinkage at the plus end, called the rescue rate r_r, and switching rate from shrinkage to growth at the plus end, called the catastrophe rate r_c, are also shown. (C) CMT zippering, when one CMT interacts with another within 40° and changes its direction to align with the other. At this angle of interaction, zippering occurs at 100% frequency. (D) Induced CMT catastrophe, when one CMT interacting with another at greater than 40° is induced to depolymerize. (E) CMT crossover, when two CMTs interact with each other at greater than 40° and cross one another. The induced catastrophes (D) and crossovers (E) each occur with a probability of 50% when CMTs meet at an angle greater than 40°. (F) CMTs with DC, which causes CMTs within the DC zone to change their direction to gradually align to a specific direction (circumferential in this study).

Fig. 2. Quantification of the cortical microtubule (CMT) band from live cell imaging data of the *Arabidopsis* zygote. (A) Two-photon excitation microscopy (2PEM) images of the time-lapse observation of a zygote expressing the MT/nucleus marker. Numbers indicate the elapsed time (h:min). Scale bar: 10 μm. (B) Schematic illustrations of zygote growth. MT, microtubule. (C) Definition of the cell centerline *S* estimated from the cell contour. (D) Quantification of the cell contour and the cell centerlines. The colors of the contours represent the time from the first frame. (E) Quantification of the CMT band. The green line indicates the width of the CMT band (defined below). (F) Truncated Gaussian fitting of the fluorescence intensity projected on the centerline (black line). The red line represents the fitted truncated Gaussian curve. The position of the CMT band μ is estimated by the median, and the width of the CMT band is estimated by σ_{MT}^{data}.. (G) Kymograph of the fluorescence intensity projected on the centerline of the zygote. The green and blue lines indicate the upper and lower limits of the CMT band, respectively, where s is the standard deviation(H) MT dynamic space (MTD space, n = 4, indicating the speed and width of the CMT bands with their frequencies (histograms)). The vertical axis denotes $\sigma_{MT}^{\mathrm{data}}$ and the horizontal axis is $d\mu_{MT}^{data}/dt$. The 95th percentile of the MTD space is shown as a pale orange region. Typical CMT patterns for the cases of the red circles are schematically illustrated.

Fig. 3. Effect of the tension-responsive ability parameter (b_d) and the width of the directional cue (DC) σ_T. (A–C) Simulation results when using no DC (A), a weak DC ($b_d = 0.001$; B), and a strong DC ($b_d = 0.01$; C). The orientation angle of the CMT measured from the horizontal axis is represented by the color used. The DC zone is indicated by black dashed lines. (D) Orientational change of a single CMT with vertical growth as a function of b_d. The DC zone is highlighted in orange. (E) Dependence of the CMT width σ_{MT}^{model} as a function of b_d. (F) Dependence of the global order parameter Λ as a function of b_d. (G, H) Results of the simulations at $t = 20$ [min] for different σ_T values in the case of a weak DC (G) and a strong DC (H). (I) Dependence of the width σ_{MT}^{model} as a function of σ_T in the case of a weak or strong DC.

Fig. 4. Effect of the cell radius R and two different types of cortical microtubule (CMT) organization. (A, B) Simulation results for a strong directional cue (DC) with a temporal dependence of Λ and σ_{MT}^{model} when $R = 5.0$ [μm] (A) and $R = 15.0$ [μm] (B). The green lines represent the sigmoid function for Λ and the linear function for σ_{MT}^{model}. (C) Schematic illustrations of rapid CMT organization. Owing to the horizontal CMTs that were rapidly organized, diagonal CMTs may be disorganized, and only the horizontal CMT band remains. The green dashed lines represent newly forming CMTs, where the red circles at the leading edge indicate those that do not collide with pre-existing CMTs, making them likely to grow. In contrast, the red crosses at the leading edge represent CMTs that collide with pre-existing CMTs, indicating a reduced likelihood of growth. The colored band represents the region under strong DC influence. (D, E) Simulation results for a weak DC with a temporal dependence of Λ and σ_{MT}^{model} when $R = 5.0$ [μm] (D) and $R = 15.0$ [μm] (E). For cases where the CMT band cannot be defined, the corresponding box plot is omitted. (F) Schematic illustrations of gradual CMT organization. The green dashed lines represent newly forming CMTs, where the red circles at the leading edge indicate those that do not collide with pre-existing CMTs, making them likely to grow. In contrast, the red crosses at the leading edge represent CMTs that collide with pre-existing CMTs, indicating a reduced likelihood of growth. The colored band represents the region under weak DC influence. Without horizontal CMTs, diagonal CMTs can be organized so that the CMT band becomes widened.

Fig. 5. Parameter inference by mapping input directional cue (DC) parameters to output the cortical microtubule (CMT) dynamic space (CDS). (A) Schematic illustrations of the microtubule dynamic (MTD) space in the data, with expected input DC parameters (green) and a similar range of input DC parameters to the MTD space (dashed line). (B) Simulated results in the CDS with the data range from Fig. 2H (green). (C) The discrepancy between the output and

input CMT speed compared with the diagonal equivalent line (gray dashed line). Depending on the output speed of the CMT band, there are static states, states that follow the input, and states that lag behind the input. (D, F, H) CMT dynamics with appropriate speed and width for the resulting CMT band (Case 01) (D), with a faster speed than the CMT band (Case 02) (F), and with a broader width and faster speed than the CMT band (Case 03) (H). (E, G, I) Schematic illustration of the obtained results. Depending on the input speed of the DC zone, the resulting CMT band did not move (E, i), moved appropriately (G, ii), or lagged behind the DC zone (I, iii).

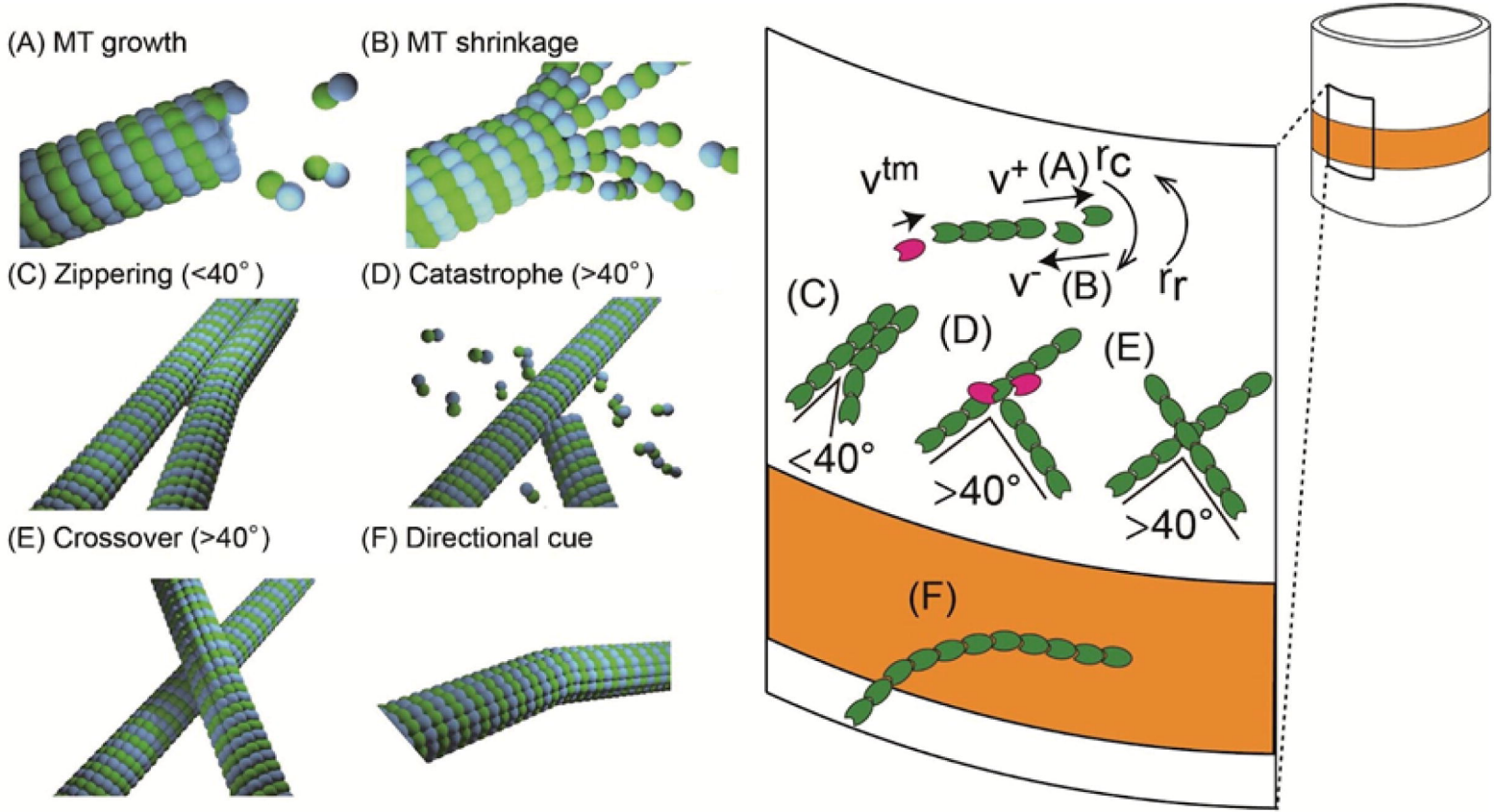
(A) MT growth
(B) MT shrinkage
(C) Zippering (<40°)
(D) Catastrophe (>40°)
(E) Crossover (>40°)
(F) Directional cue
v^tm
v^+ (A)
r^c
v^- (B)
r^r
(C)
(D)
(E)
<40°
>40°
>40°
(F)

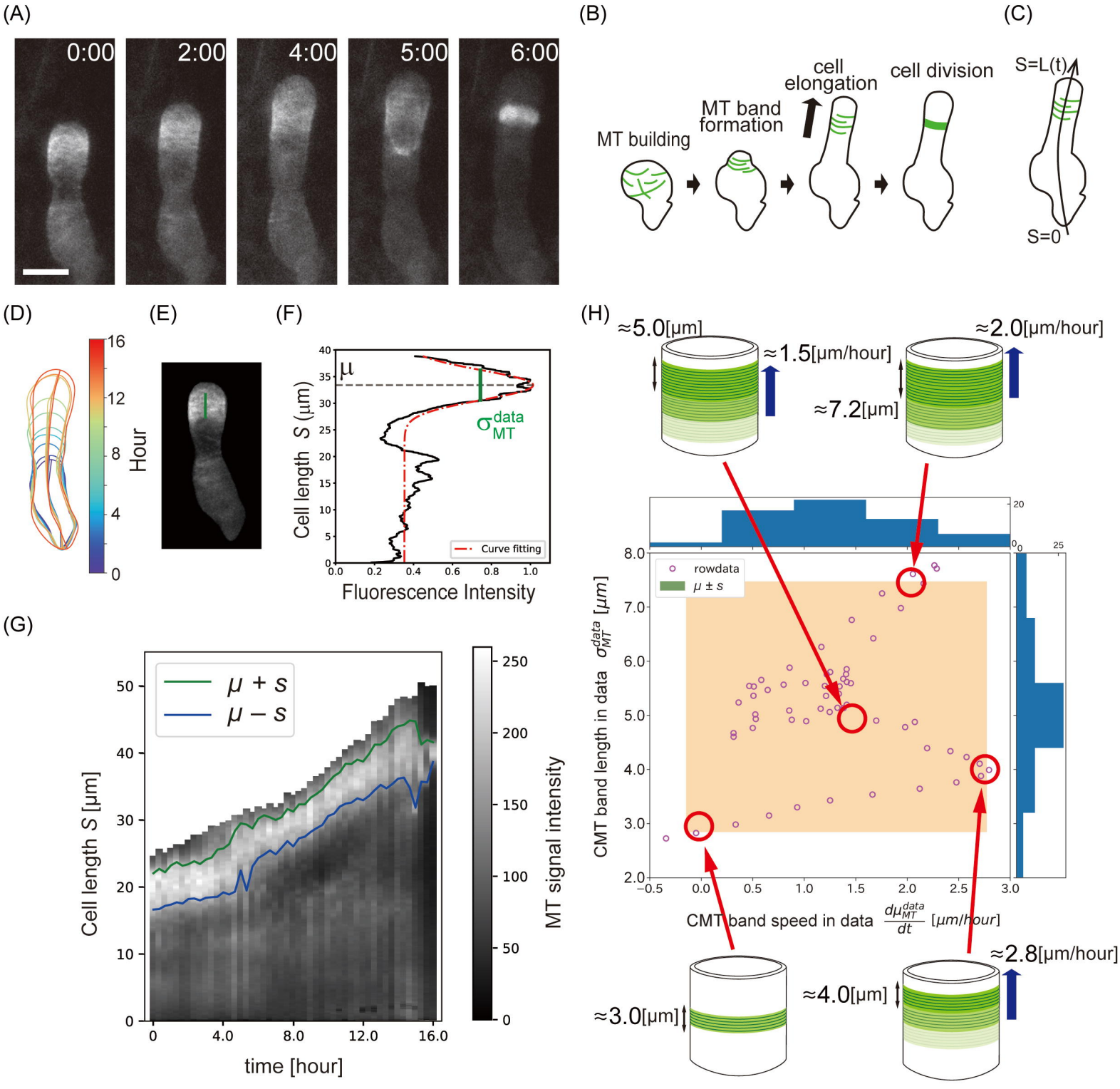
(A)
0:00
2:00
4:00
5:00
6:00
(B)
MT building
MT band formation
cell elongation
cell division
(C)
S=L(t)
S=0
(D)
Hour
(E)
(F)
μ
σ_{MT}^{data}
Curve fitting
Cell length S (μm)
Fluorescence Intensity
(G)
μ + s
μ − s
Cell length S [μm]
time [hour]
MT signal intensity
(H)
≈5.0[μm]
≈1.5[μm/hour]
≈2.0[μm/hour]
≈7.2[μm]
rowdata
μ ± s
CMT band length in data σ_{MT}^{data} [μm]
CMT band speed in data $\frac{d\mu_{MT}^{data}}{dt}$ [μm/hour]
≈3.0[μm]
≈4.0[μm]
≈2.8[μm/hour]

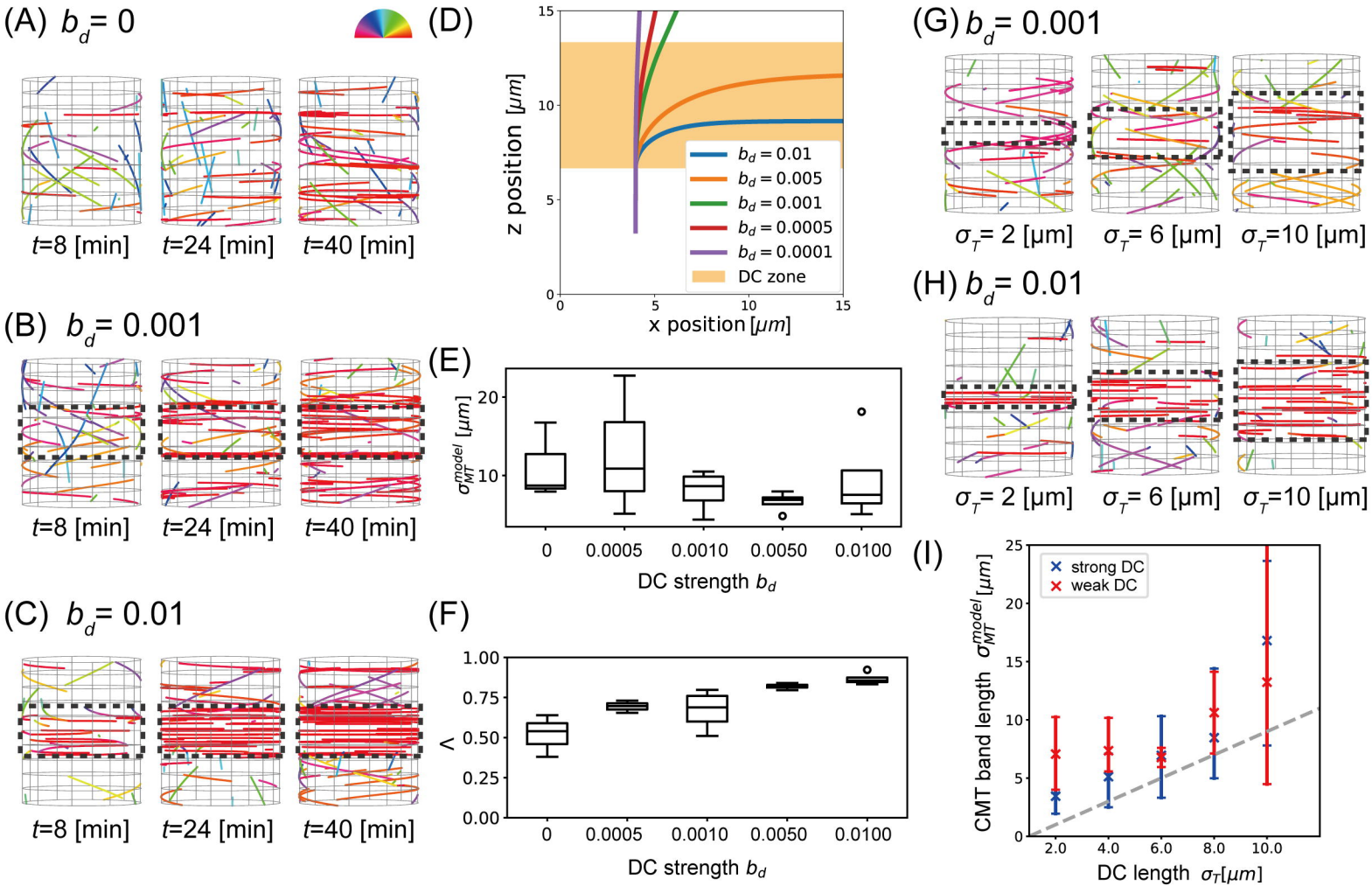
(A) b_d= 0
t=8 [min]
t=24 [min]
t=40 [min]
(B) b_d= 0.001
t=8 [min]
t=24 [min]
t=40 [min]
(C) b_d= 0.01
t=8 [min]
t=24 [min]
t=40 [min]
(D)
z position [μm]
x position [μm]
b_d = 0.01
b_d = 0.005
b_d = 0.001
b_d = 0.0005
b_d = 0.0001
DC zone
(E)
σ_{MT}^{model} [μm]
DC strength b_d
(F)
<
DC strength b_d
(G) b_d= 0.001
σ_T= 2 [μm]
σ_T= 6 [μm]
σ_T=10 [μm]
(H) b_d= 0.01
σ_T= 2 [μm]
σ_T= 6 [μm]
σ_T=10 [μm]
(I)
strong DC
weak DC
CMT band length σ_{MT}^{model} [μm]
DC length σ_T[μm]

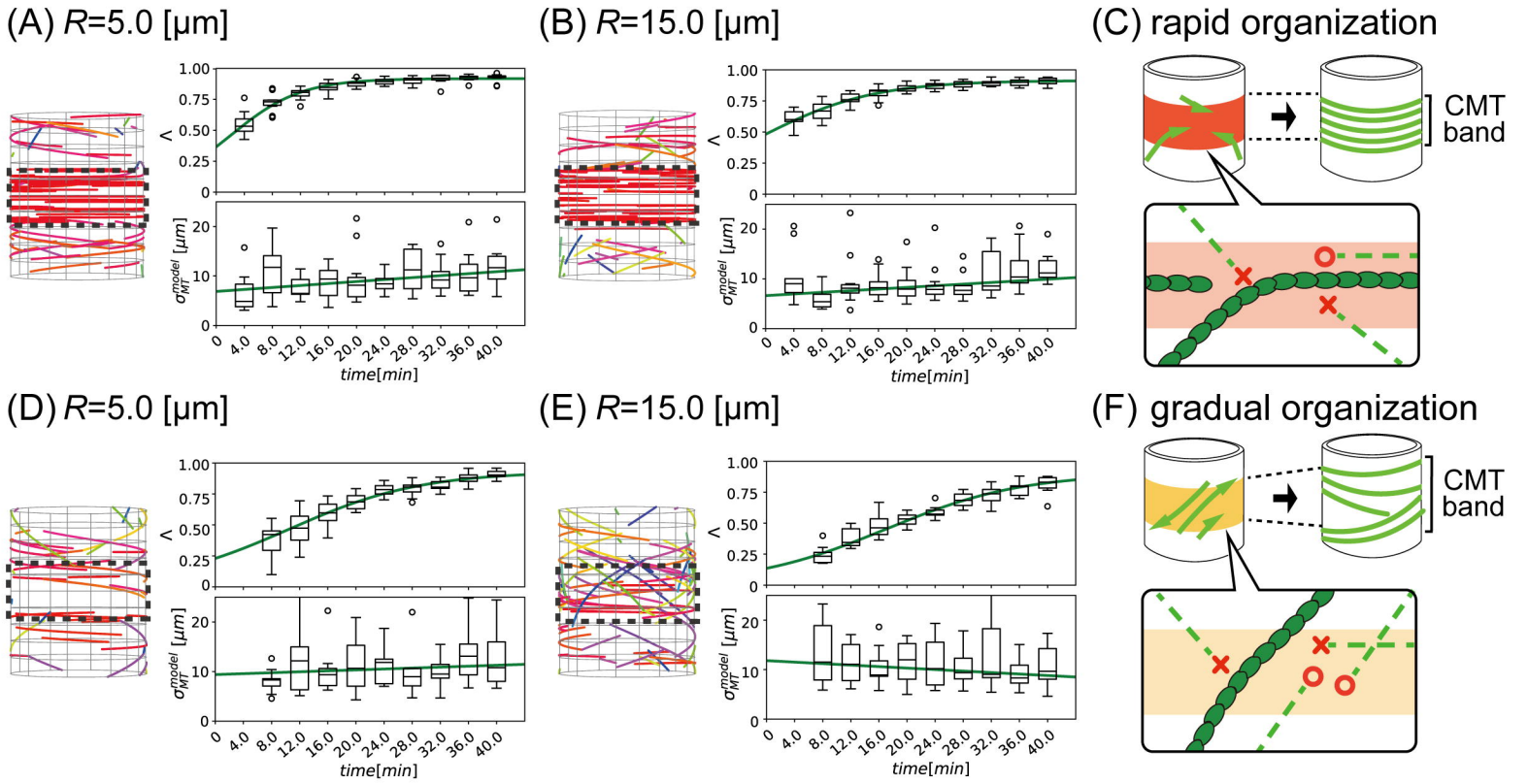
(A) R=5.0 [μm]
(B) R=15.0 [μm]
(C) rapid organization
CMT band
(D) R=5.0 [μm]
(E) R=15.0 [μm]
(F) gradual organization
CMT band
time[min]

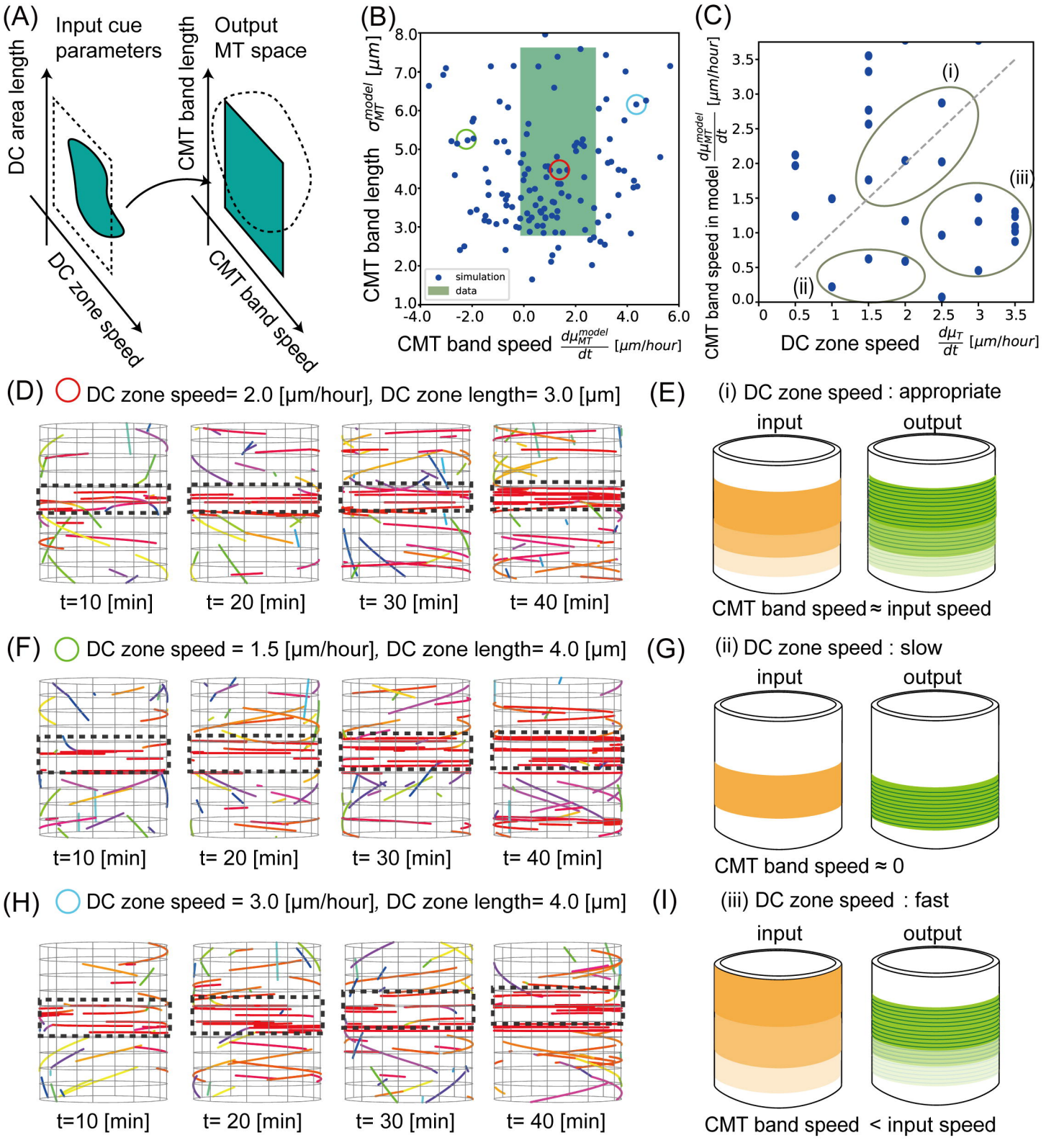
(A)
Input cue parameters
Output MT space
DC area length
CMT band length
DC zone speed
CMT band speed
(B)
CMT band length σ_{MT}^{model} [μm]
CMT band speed $\frac{d\mu_{MT}^{model}}{dt}$ [μm/hour]
simulation
data
(C)
CMT band speed in model $\frac{d\mu_{MT}^{model}}{dt}$ [μm/hour]
DC zone speed $\frac{d\mu_T}{dt}$ [μm/hour]
(i)
(ii)
(iii)
(D) DC zone speed= 2.0 [μm/hour], DC zone length= 3.0 [μm]
t=10 [min]
t= 20 [min]
t= 30 [min]
t= 40 [min]
(E) (i) DC zone speed : appropriate
input
output
CMT band speed ≈ input speed
(F) DC zone speed = 1.5 [μm/hour], DC zone length= 4.0 [μm]
t=10 [min]
t= 20 [min]
t= 30 [min]
t= 40 [min]
(G) (ii) DC zone speed : slow
input
output
CMT band speed ≈ 0
(H) DC zone speed = 3.0 [μm/hour], DC zone length= 4.0 [μm]
t=10 [min]
t= 20 [min]
t= 30 [min]
t= 40 [min]
(I) (iii) DC zone speed : fast
input
output
CMT band speed < input speed